Enhanced strength-ductility combination in the aluminum-gold system by heterogeneous distribution of nanoparticles via ultra-severe plastic deformation and reactive interdiffusion

Abbas Mohammadi, Xavier Sauvage, Fabien Cuvilly, Kaveh Edalati

To cite this version:

Abbas Mohammadi, Xavier Sauvage, Fabien Cuvilly, Kaveh Edalati. Enhanced strength-ductility combination in the aluminum-gold system by heterogeneous distribution of nanoparticles via ultra-severe plastic deformation and reactive interdiffusion. Journal of Materials Science and Technology, 2024, 203, pp.269 - 281. ⟨10.1016/j.jmst.2024.03.049⟩. ⟨hal-04607356⟩

Enhanced strength-ductility combination in the aluminum-gold system by heterogeneous distribution of nanoparticles via ultra-severe plastic deformation and reactive interdiffusion

Abbas Mohammadi[1], Xavier Sauvage[2], Fabien Cuvilly[2], Kaveh Edalati[1,]*

[1]WPI, International Institute for Carbon-Neutral Energy Research (WPI-I2CNER), Kyushu University, Fukuoka, Japan
[2]Univ Rouen Normandie, INSA Rouen Normandie, CNRS, Groupe de Physique des Mat´eriaux, UMR6634, 76000 Rouen, France

Ultrafine-grained aluminum alloys are of interest due to their high strength-to-weight ratio, but they usually suffer from poor uniform ductility. In this study, an Al-Au alloy with a good combination of strength and ductility is produced by the heterogeneous distribution of Al_2Au nanoparticles in an aluminum matrix. To generate such heterogeneity, the alloy is synthesized by ultra-severe plastic deformation of aluminum and gold powders via the high-pressure torsion method. Reactive interdiffusion occurs during the process leading to the heterogeneous formation of intermetallic particles and a good strength-ductility synergy (200 MPa yield stress and 15% uniform elongation). Nanoparticles gradually distribute within the matrix and once a uniform nanoparticle distribution is achieved, the alloy shows no further increase in strength, but it completely loses its ductility. It is concluded that not only the presence of nanoparticles but more importantly the heterogeneity of their distribution can positively influence the strength-ductility combination in ultrafine-grained aluminum alloys. The findings of this study suggest that future studies on heterogeneous precipitation hardening can be a solution to achieve ductile precipitation-hardened alloys.

Keywords: precipitate hardening, ultrafine-grained (UFG) materials, severe plastic deformation, aluminum alloy, mechanical strength

*Corresponding authors:
Kaveh Edalati (E-mail: kaveh.edalati@kyudai.jp, Tel/Fax: +81-92-802-6744)

Cite as :

Abbas Mohammadi, Xavier Sauvage, Fabien Cuvilly, Kaveh Edalati

Enhanced strength-ductility combination in the aluminum-gold system by heterogeneous distribution of nanoparticles via ultra-severe plastic deformation and reactive interdiffusion

Journal of Materials Science & Technology, Volume 203, 2024, Pages 269-281, https://doi.org/10.1016/j.jmst.2024.03.049.

1. Introduction

Metals and alloys with ultrafine-grain sizes exhibit high strength due to the Hall-Petch strengthening mechanism [1]. Such strengthening leads to a desirable enhancement of the strength-to-weight ratio, particularly for light metals such as magnesium [2], aluminum [3] and titanium [4]. However, ultrafine-grained metals and alloys usually exhibit limited uniform elongation due to limitations in the dislocation accumulation and resultant minimal strain hardening capability [5]. To overcome the strength-ductility trade-off relationship in ultrafine-grained metals, different strategies were employed: nanotwinning [6,7], gradient nanostructuring [8,9], composition control for lattice softening [10,11], bimodal microstructure formation [12,13], introduction of lamellar microstructure [14,15], controlled precipitation hardening [16,17], twinning-induced plasticity (TWIP) [18,19] and transformation-induced plasticity (TRIP) [20,21].

With the fast development of severe plastic deformation (SPD) to produce ultrafine-grained metals [22,23], some researchers focused on the enhancement of ductility by controlling SPD processing [24,25]. Although there has been limited success in this regard, it is well documented that SPD is capable of controlling microstructure for achieving a desirable property [22,23]. One of the recent attempts to develop materials with high strength and high ductility is the development of heterostructured materials by SPD [26]. In heterostructured materials, usually, a combination of nanograined and coarse-grained microstructures is generated in the microstructure [27]. It is believed that the nanograined phase enhances the strength, but the coarse-grained phase contributes to the ductility by accumulating dislocations [26,27]. Despite significant studies on the effect of heterogenous grain size distribution on the strength-ductility combination, clarification of the effect of other heterogeneities such as compositions, defects (dislocations, twins, stacking faults) and second phase distribution (particles and precipitates) needs further investigations. Regarding the second-phase particle distribution, it should be noted that the conventional precipitation hardening process usually results in a homogenous distribution of nanoparticles [28,29]. Although the heterogeneous distribution of nanoprecipitates reported in some special cases such as in thin films [30], medium-entropy alloys [31], high-entropy alloys [32], shape memory alloys [33] and additively manufactured alloys [34], new strategies are still needed to be employed to achieve heterogeneous precipitation hardening.

In this study, it is hypothesized that the heterogeneous distribution of nanoparticles is as effective as the heterogeneous grain size distribution in achieving high ductility in nanostructured alloys. To examine this issue, an Al-Au model system is selected and synthesized by mechanical alloying of aluminum powders with a small fraction of gold through severe plastic deformation to achieve microstructures with heterogeneous and homogeneous distributions of intermetallic intermetallic nanoparticles. The reasons for the selection of this unusual system and such a processing method are explained here. (i) Aluminum and gold both exhibit FCC structures with very similar lattice parameters and reasonably close hardness which promotes their co-deformation [35]. The very limited size mismatch between aluminum and gold atoms minimizes also the risk of segregation along crystalline defects as observed in other Al-based systems [36]. These similarities should promote the reaction between aluminum and gold during deformation; (ii) Unlike copper and silver with FCC structures similar to aluminum, the solubility of gold in aluminum is negligible up to the melting point and the Al-Au phase diagram indicates only the formation of intermetallics (Al_2Au, AlAu, $AlAu_2$, Al_2Au_5 and $AlAu_4$) [35]. Such immiscibility is beneficial to limit the formation of supersaturated solid solutions and promote the reaction at Al/Au interfaces [37,38]. (iii) SPD by high-pressure torsion (HPT) is a relatively fast method for mechanical mixing of heterogenous metal-metal mixture [37] and it can be successfully applied to extreme shear strains over 1000 (called ultra-SPD [38]) which are eventually necessary to homogenize the distribution of second-phase particle. This process has been applied to various immiscible Al-based systems such as Al-Fe [39], Al-Ca [40], Al-Zr [41] and Al-La-Ce [42], although as-cast structures already containing intermetallic phases were usually processed. In the present study, we show that the appropriate selection of the Al-Au system makes it possible to achieve progressively a high density of nanoscaled intermetallic particles. The nanoparticle distribution, which evolves as a function of strain level, has a significant effect on the strength-ductility trade-off.

2. Experimental Procedures

To produce the unique microstructure of the Al-Au alloy of the present study, powder of aluminum (99.99%) was mixed with 1 mol% of gold powder (99.99%) in acetone (powder sizes were smaller than 45 μm). After mixing for 30 minutes, acetone was evaporated and the dried powder mixture was compressed to discs with 10 mm diameter and 0.9 mm thickness under a pressure of 380 MPa. The compressed discs were processed by high-pressure torsion (HPT) under a pressure of 6 GPa at room temperature for 1, 10,100 and 1000 rotations with a speed of 1 rotation per minute. A schematic illustration of the HPT process is shown in Fig. 1a and its details can be found in a review paper [43]. The samples after HPT were evaluated by different methods, as shown in Fig. 1b.

First, for the assessment of solid-state reactions and phase transformation, X-ray diffraction was employed. The discs were mechanically polished on both upper and lower surfaces to mirror-like quality and analyzed by XRD using a Cu Kα X-ray source. The acceleration voltage was 45 kV, the anode current was 40 mA, and the scanning step and speed were 0.05° and of 2 $^{\circ}$/min, respectively. The XRD profiles were analyzed using a PDXL software equipped with the Rietveld refinement method.

For evaluation of hardness, the upper mirror-like surface of the discs was examined by Vickers microhardness measurement. Hardness was measured at four radial positions from the disc center to the periphery at distances of 0.15, 1, 2, 3 and 4 mm from the center. The applied load for hardness measurement was 5 N and the dwell time was 15 s. The hardness values were analyzed as a function of shear strain, as attempted earlier [44,45], where the shear strain was calculated using the following relationship [46].

$$\gamma = 2\pi rN/h \quad (1)$$

In this relationship, r, N and h are radial distance from the disc center, the number of HPT rotations and the disc height, respectively.

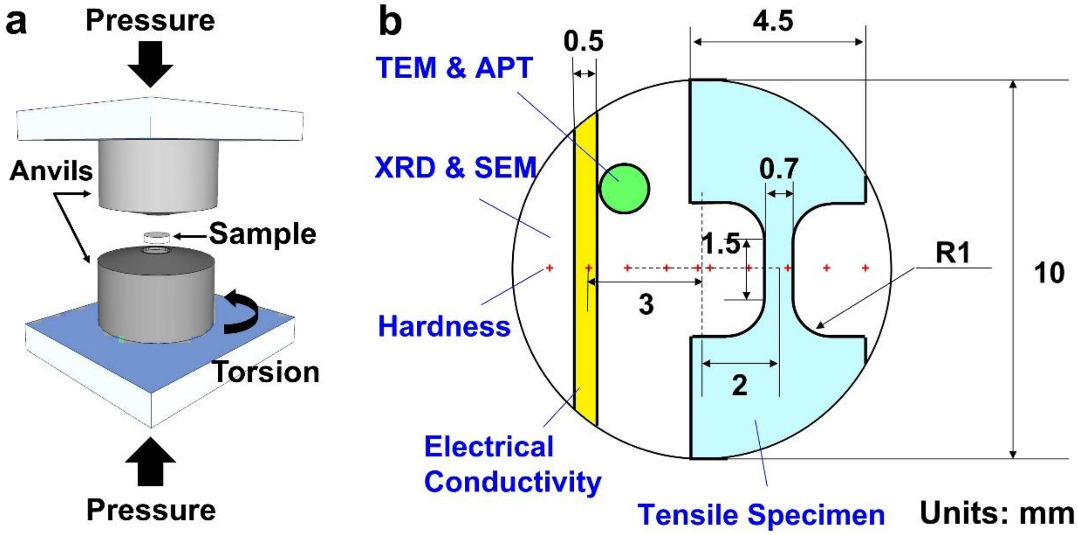

Fig. 1. Schematic illustration of (a) HPT and (b) procedures used for conducting different characterization methods.

As another tool to examine the evolution of microstructure with strain, electrical conductivity measurements were conducted following the procedure described earlier [41,42]. Rods with 0.6×0.6 mm^2 cross-section were cut at 3 mm away from the center of HPT discs and their electrical resistivity was measured using a four-point probe approach. A current of 100 mA was applied and the voltage was measured within a central length of 4 mm. The electrical resistivity was then calculated by dividing the voltage by current and the electrical conductivity was determined as $K = 172.41/\rho$, where K is the conductivity in %IACS (international annealed copper standard) and ρ is the resistivity in μΩ.cm.

For examination of the strength and ductility relationship, miniature dog-bone type tensile specimens with 1.5 mm gauge length, 0.6 mm gauge width and 0.6 mm gauge thickness were prepared from the disc samples using an electric discharge machine. The position of the center of the gauge was located at 2 mm from the disc center, as shown in Fig. 1b. The tensile specimens were pulled to failure under a constant displacement speed with an initial strain rate of 5.5×10^{-4} s^{-1}. The fracture surfaces of tensile specimens were examined by scanning electron microscopy (SEM) in secondary electron mode and back-scatter electron mode using an acceleration voltage of 15 kV.

For microstructural examinations, the mirror-like surfaces of discs were examined by SEM in back-scatter electron mode using an acceleration voltage of 15 kV at the center of the disc (r = 0), middle of the disc (r = 2.5 mm) and the edge of the disc (r = 5.0 mm). In addition to conventional SEM observations, energy-dispersive X-ray spectroscopy (EDS) was conducted to detect the distribution of elements at the micrometer level.

For nanostructural examinations, transmission electron microscopy (TEM) and scanning-transmission electron microscopy (STEM) were conducted using a JEOL ARM 200F microscope. Thin foils were prepared in the cross-section of the HPT discs using the focused ion beam (FIB) method at about 3.5 mm away from the disc center and examined by TEM and STEM. The acceleration voltage for TEM and STEM was 200 kV and the samples were analyzed by different modes such as bright field (BF), dark field (DF), selected area electron diffraction (SAED), STEM bright field (STEM-BF) and high-angle annular dark field (HAADF).

Collection angles for STEM-BF and HAADF were, 0-45 mrad and 68-280 mrad, respectively. Energy Dispersive X-ray Spectroscopy (EDS) was also carried out for chemical analyses using a JEOL Centurio detector with a collection angle of 1 sr. Average grain sizes were determined from TEM and STEM micrographs for over 100 grains.

For investigation of the distribution of elements at the atomic scale, atom probe tomography (APT) was employed. APT samples were picked up at 3.5 mm from the disc center using the FIB method. APT analysis was conducted using a CAMECA LEAP-4000HR instrument under ultra-high vacuum (10^{-11} mbar) at a cryogenic temperature of 40 K. The frequency of pulses for evaporation and ionization was 200 kHz and the pulse fraction was 20%. Analyzed volumes were reconstructed using IVAS–(Integrated Visualization & Analysis Software), and data analysis was carried out using Gpm3dSoft (Groupe de Physique des Matériaux 3D-soft) software.

3. Results

3.1. Structural and Microstructural Evolution

The evolution of solid-state reactions and crystal structure is shown in Fig. 2. Fig. 2a shows that only one FCC phase is detected in the initial sample. Since the crystal structure and lattice parameters of aluminum and gold are so similar [35], it is hard to distinguish them using XRD analysis. After HPT processing, two main changes occur. First, peaks corresponding to the FCC phase become slightly broader, as shown more clearly in a magnified view in Fig. 2b. Peak broadening is an indication of lattice strain, dislocation generation and crystallite size reduction [47], a fact that was reported frequently after SPD processing [48,49]. Second, peaks corresponding to the Al_2Au intermetallic phase appear after 10 turns with an increase in intensity when the number of rotations becomes larger, as shown more clearly in Fig. 2c. The fraction of Al_2Au calculated using the Rietveld method is shown against the number of HPT turns in Fig. 2d. While the fraction of phase is almost zero after 1 turn, it increases to 0.54, 1.00 and 7.77 wt% after 10, 100 and 1000 turns, respectively. A comparison between the fraction of 7.77 wt% achieved after 1000 turns and the phase diagram of the Al-Au system [35] suggests that about 1wt% of gold should be in the solid-solution form. Such solid-state reactions and dissolution of elements in each other have been reported in some cases during SPD processing [50] and seem more frequent after ultra-SPD due to the severity of deformation [51].

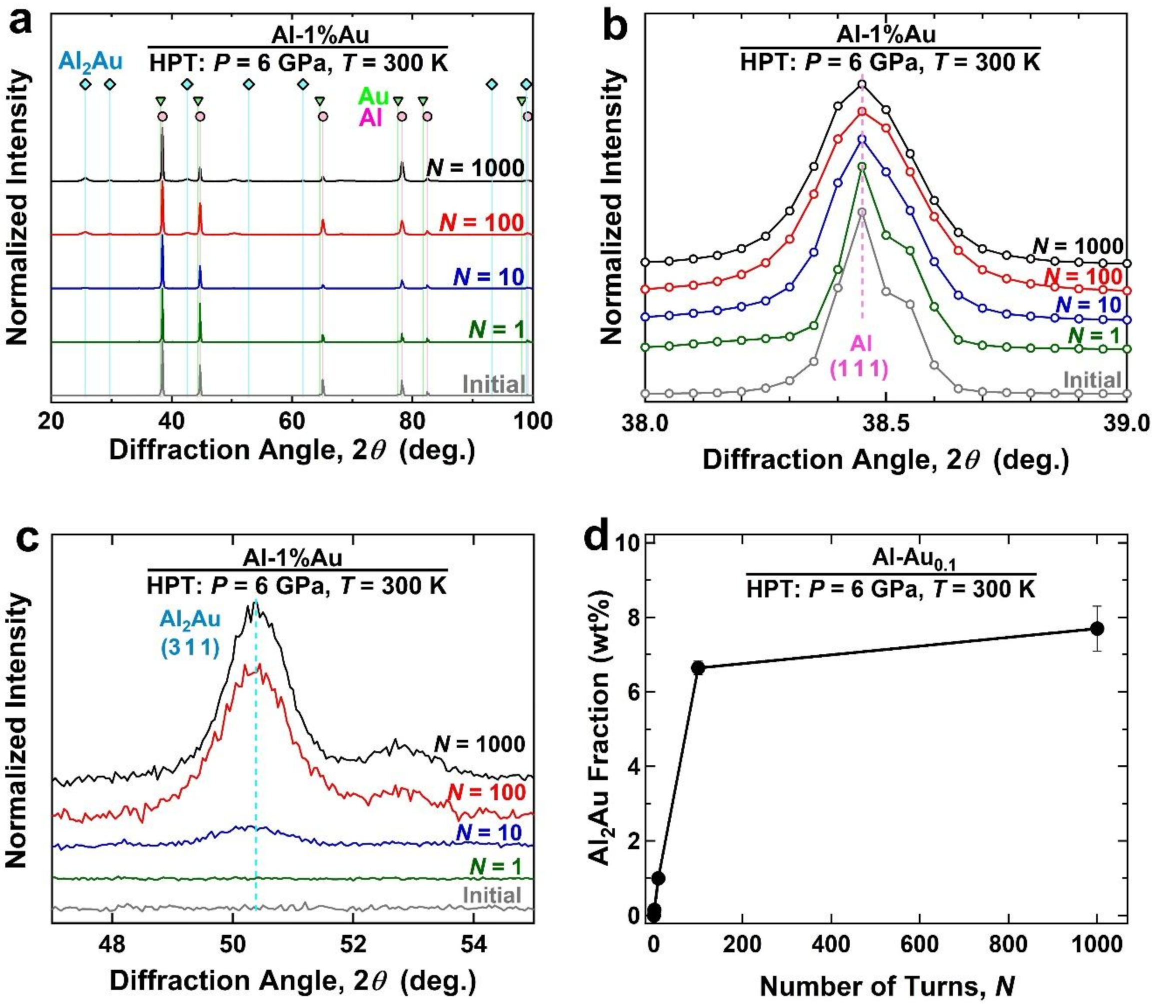

Fig. 2. XRD spectra of Al - 1 mol% Au before and after HPT processing with 1, 10, 100 and 1000 rotations: (a) overall view, (b) magnified view of the (111) peak of aluminum and (c) magnified view of the (311) peak of Al_2Au. (d) Al_2Au phase fraction calculated from XRD spectra using Rietveld method.

The evolution of microstructure was first examined by SEM using back-scatter electron mode and EDS, as shown in Fig. 3a, for the center, middle and edge of HPT-processed discs (i.e. at r = 0, 2.5 and 5.0 mm from the center of HPT-processed discs). For the sample processed with 1 rotation, minor co-deformation of aluminum and gold particles is observed at the center, middle or edge of the disc. After 10 rotations, the center of the disc still shows isolated gold particles within the aluminum matrix, but the co-deformation of aluminum and gold is clearly observed at the middle and edge of disc samples. After 100 turns, two phases (Au-rich and Au-poor) are still detected at the center of the disc, while the microstructure looks more homogeneous at the middle and edge of the disc. The Al-rich and Al-poor regions cannot be distinguished at low magnification after 1000 rotations. Examination at higher magnifications (Fig. 3b), clearly shows however that nanoscaled Au-rich nanoparticles are embedded in the Al matrix. Considering XRD spectra (Fig. 2) these nanoparticles should be mostly the Al_2Au intermetallic.

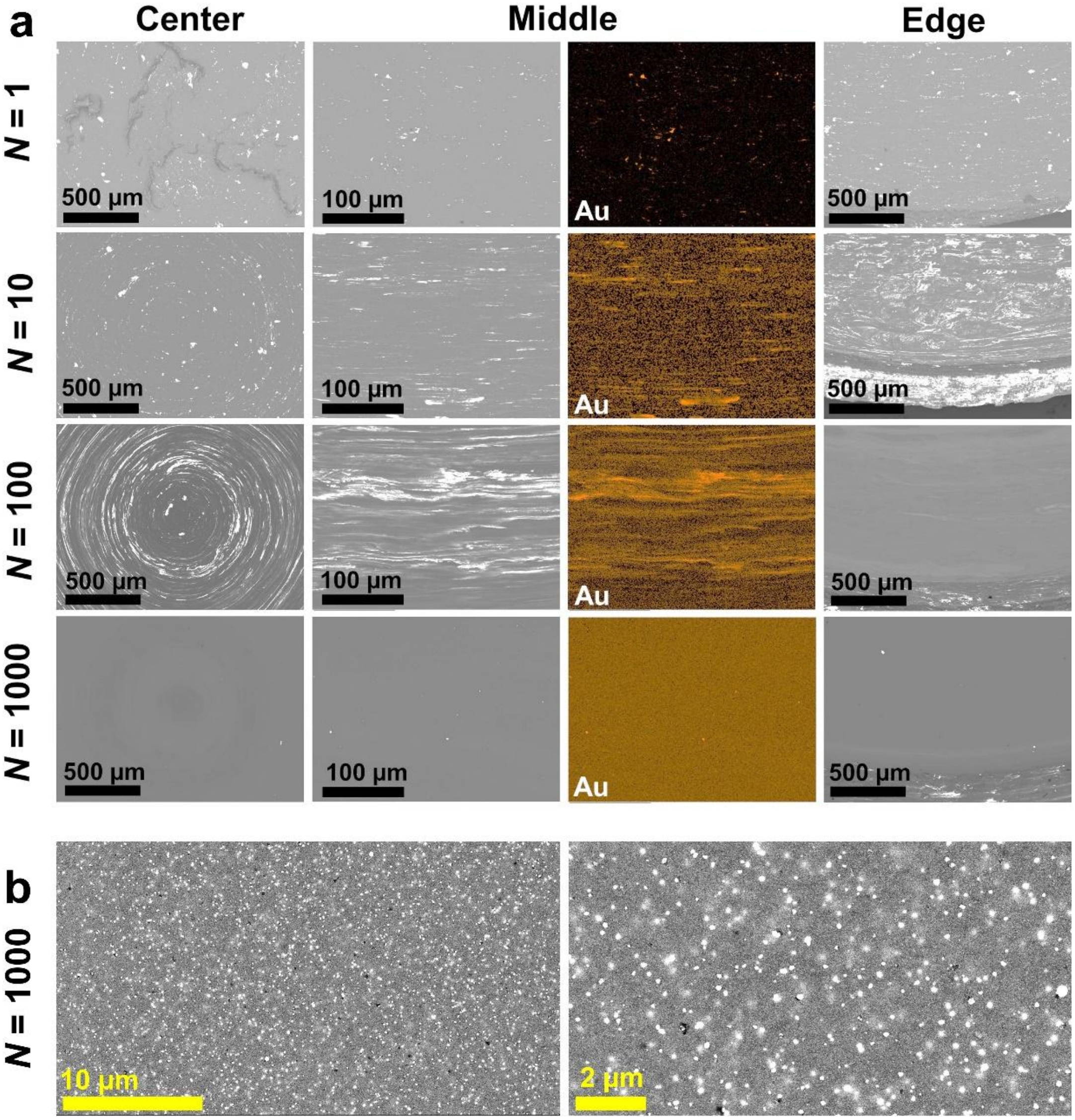

Fig. 3. (a) SEM micrographs taken from disc center, middle and edge and EDS mapping with gold taken from disc middle for Al - 1 mol% Au after HPT treatment with 1, 10, 100 and 1000 rotations, and (b) high-magnification SEM back-scatter electron images taken from disc edge for sample processed with 1000 rotations. Center, middle and edge refer to r = 0, 2.5 and 5.0 mm from the center of HPT-processed discs, respectively.

To collect more precise information about the microstructure evolution during HPT processing, TEM and STEM observations were conducted. Typical images of the samples deformed by 10, 100 and 1000 HPT rotations are shown in Fig. 4 and Fig. 5. Details concerning these images are discussed below.

At moderate deformation (10 HPT revolutions), an ultrafine-grained structure is clearly exhibited in the aluminum matrix on the STEM-DF image (Fig. 4a) with a mean grain size of 220 nm. Gold particles that appear bright on STEM-HAADF images (Fig. 4b) have been strongly elongated along the shear direction (horizontal) with a thickness ranging from 50 to 300 nm. The shear deformation theoretically leads to thickness *L* which is written as [51]:

$$L = d_0/\gamma \tag{2}$$

where d_0 is the initial particle size (~10 μm) and γ is the shear strain (estimated from Eq. 1). Then, after 10 HPT revolutions at 2 mm from the disc center, L = 70 nm which is significantly smaller than observations. However, as shown on XRD spectra (Fig. 2c) and confirmed by EDS analyses (Fig. 4c and Fig. 4d), some reactive interdiffusion occurred at Al/Au interfaces. There is no more gold phase and two intermetallic phases have formed, the Al_2Au phase (33 at% Au) on the aluminum side and the AlAu phase (50 at% Au) on the gold side. Thus, the thickness of Au-rich layers appears larger than expected because of these reactions. Surprisingly, the AlAu phase could not be detected by XRD. This is attributed to a relatively low volume fraction. Some Kirkendall voids are also clearly exhibited with a dark contrast in the core of the Au-rich layers (Fig. 4b). They are typical in many systems after reactive interdiffusion and result from a difference in the diffusion coefficient of the two elements [52]. In the present case, the probability of the exchange of a vacancy with a gold atom is larger than that of an exchange with an aluminum atom [53]. Although the co-deformation of aluminum and gold proceeds relatively smoothly, Au-rich layers do not exhibit a continuous and homogeneous thickness (Fig. 4b). Some of them are fragmented in nanoscaled particles forming clusters in the Al matrix (Fig. 4e). The SAED pattern (Fig. 4e inset) confirms that they are Al_2Au particles, the intermetallic with the highest amount of Al expected from the phase diagram [35].

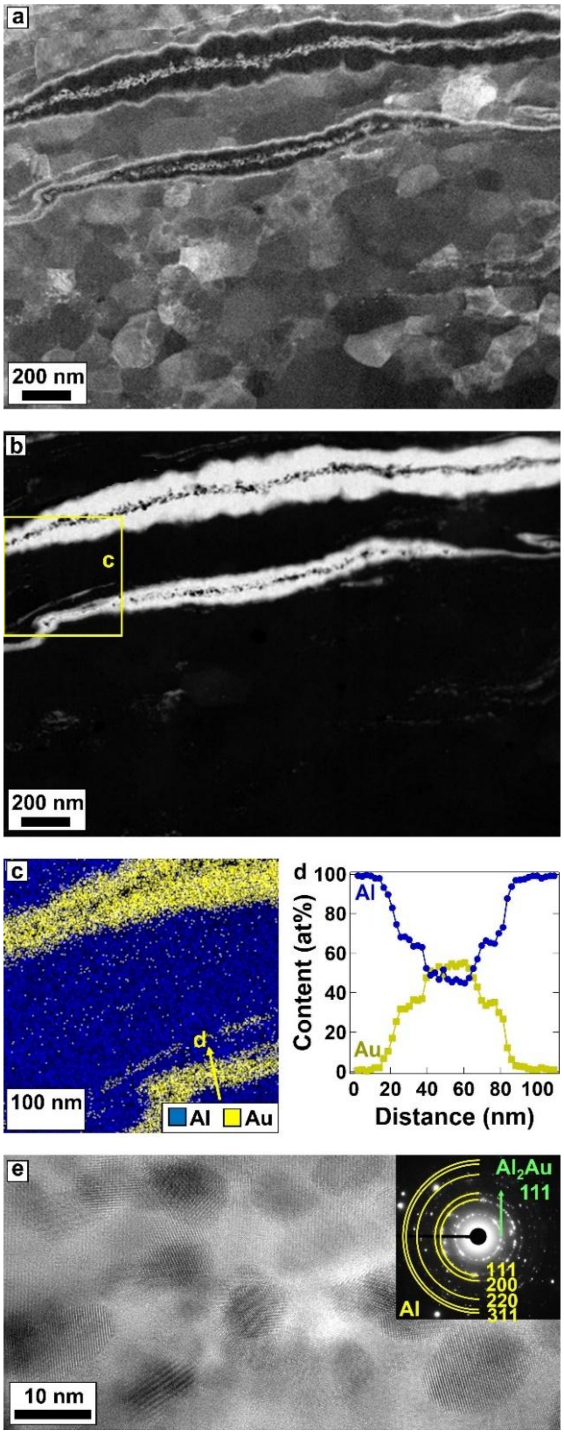

Fig. 4. Microstructural evolution for Al - 1 mol% Au after HPT treatment with 10 rotations: (a) STEM-DF image, (b) STEM-HAADF image, (c) EDS mapping taken from the square region shown in (b) micrograph, (d) EDS line profile along arrow shown in (c) mapping, and (e) TEM high-resolution lattice image of Au-rich phase and corresponding SAED pattern.

The evolution of microstructure after 100 and 1000 rotations of HPT is compared in Fig. 5 using (a, b) TEM-BF, (c, d) SAED, (e, f) STEM-BF and (g, h) STEM-HAADF. The average grain size in the aluminum matrix only slightly decreases with further deformation beyond 10 revolutions: 220 nm for N = 10, 190 nm for N = 100 nm and 170 nm for N = 1000. Al_2Au nanoscaled particles are clearly exhibited after 100 and 1000 HPT revolutions (structure confirmed by SAED patterns) which is consistent with XRD data (Fig. 2). The distribution of these particles is affected by the deformation, and it becomes homogenous after 1000 HPT rotations. The average particle size is 10 nm and their sizes and shape are relatively similar at deformation levels of 100 and 1000 rotations.

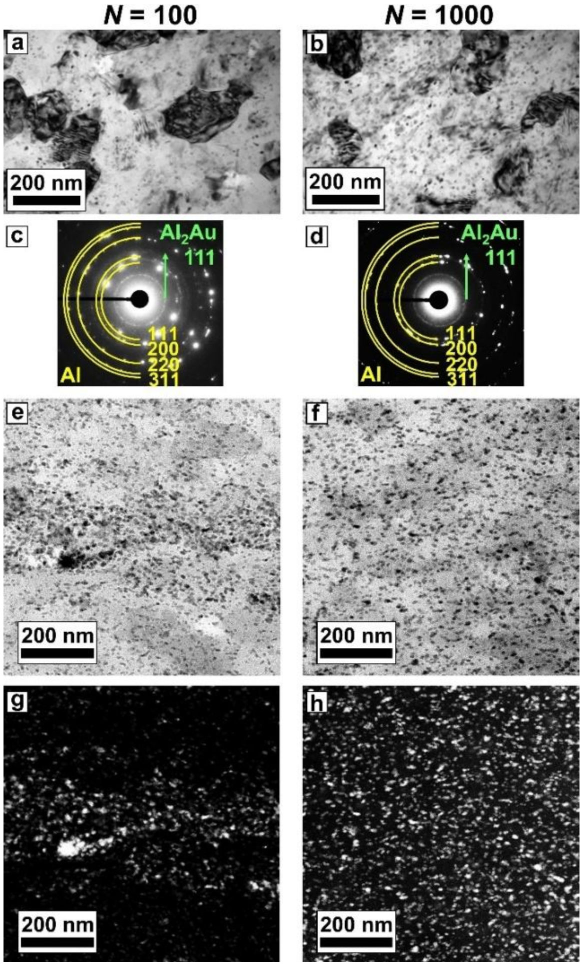

Fig. 5. Microstructural evolution for Al - 1 mol% Au after HPT treatment with (a, c, e, g) 100 rotations and (b, d, f, h) 1000 rotations: (a, b) TEM-BF image, (c, d) SAED patterns, (e, f) STEM-BF images, and (g, h) STEM-HAADF images.

The detailed features of the nanoscaled particles examined by STEM and APT are summarized in Fig. 6. STEM-HAADF and corresponding EDS mapping in Fig. 6a and 6b, respectively, illustrate that they are distributed within aluminum ultrafine grains and not specifically along defects such as grain boundaries. High-resolution HAADF and corresponding fast Fourier transform (FFT) diffractograms in Fig. 6c and 6d indicate that nanoparticles exhibit the Al_2Au crystal structure and that they have no preferred orientation or coherency with the aluminum matrix. Such a feature is relatively unique since usually in precipitate-hardening alloys, nanoparticles that result from a classical precipitation process (involving nucleation and growth) exhibit some specific orientation relationships [16,17]. Atomic-scale analysis using APT (Fig. 6e and 6f and supplementary video) provides more details about the distribution of gold atoms and the three-dimensional morphology of nanoscaled particles. The composition of the volume exhibited in Fig. 6e is 1.07±0.01 at% Au, close to the nominal composition, indicating that even if the volume is small, it is fully representative. The average amount of gold measured in the aluminum matrix is 0.13±0.01 at%, which is higher than the room temperature solubility of gold in aluminum (0.06 at% Au [35]), indicating that SPD promoted the formation of slightly supersaturated solid solution as revealed in other systems [39-42]. The amount of 0.13 at% of gold which is equivalent to 0.94 wt% is consistent with the value predicted from the Rietveld refinement method (~1 wt%). The amount of gold in the core of nanoscaled particles is close to 30 at% as expected for the Al_2Au structure. No grain boundary segregation of gold was detected by APT or STEM-EDS, which is a significant difference as compared to other immiscible Al-based systems processed by SPD. This might be attributed to the very small size mismatch between gold and aluminum, and thus a small interaction of gold with elastic fields of dislocations. Besides, the kinetics of the reaction between aluminum and gold atoms at Al/Au interphases being fast, gold atoms seem to have little chance of being captured by crystalline defects in aluminum grains at Al/Au interfaces [53].

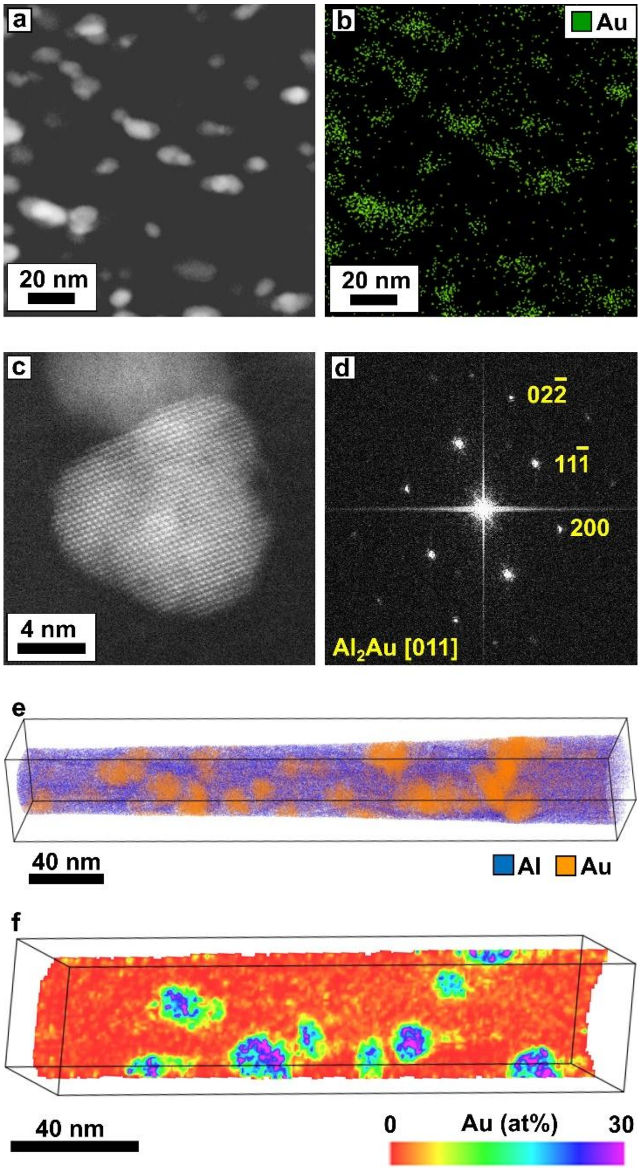

Fig. 6. Nanoscaled particles in Al - 1 mol% Au after 1000 HPT rotations: (a) STEM-HAADF image, (b) EDS mapping corresponding to (a) micrograph, (c) high-resolution STEM-HAADF lattice image of an isolated particle, (d) FFT diffractogram corresponding to (c) image, (e) three-dimensional volume analyzed by APT showing the distribution of aluminum and gold, (f) two-dimensional gold concentration map across a subsection of the volume displayed in (e).

3.2. Mechanical Property Evolution

Since hardness measurement provides a fast assessment for microstructural evaluation during HPT [44-46], hardness values were measured and plotted against distance from the disc center (Fig. 7a) and shear strain (Fig. 7b). The hardness increases with increasing the distance from the disc center and with increasing the number of turns, but the hardness after 1000 turns saturates to the steady state. These variations can be rationalized to the shear strain, as shown in Fig. 7b, in which hardness increases with increasing shear strain and saturates to the steady state at shear strains over 3000. This hardness-strain behavior is similar to many HPT-processed materials [24,44]; however, the main difference is that a real steady state appears at extremely large strains after ultra-SPD. This is attributed to the final stage of the microstructure evolution, after the reactive interdiffusion and full homogenization of the Al_2Au nanoscaled particle distribution. The appearance of saturation at extremely large strains after ultra-SPD was reported in other Al-based alloys [39,40,42], while some of them like Al-Zr do not show a saturation even after imposing shear strains up to 60,000 [41].

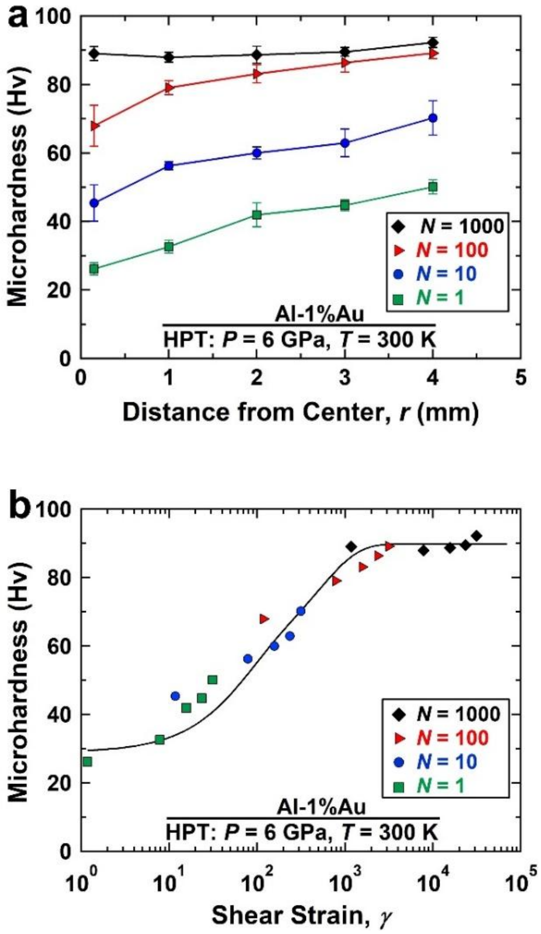

Fig. 7. Vickers microhardness versus (a) distance from disc center and (b) shear strain for Al - 1 mol% Au after HPT treatment with 1, 10, 100 and 1000 rotations.

Tensile stress-strain curves are shown in Fig. 8 for samples processed by HPT for different numbers of rotations. For the sample processed by HPT for 1 rotation, the yield stress is about 120 MPa, and there is no strain hardening. The tensile behavior for this sample, including yield stress level and negligible uniform ductility, is quite similar to the tensile curve reported for pure aluminum (99.99%) after SPD processing [54]. This similarity between the tensile properties of pure aluminum and the Al-Au alloy after 1 rotation is expected from the rule of mixtures because no appreciable mechanical alloying proceeds after 1 rotation and the sample can be considered as a composite of SPD-processed pure aluminum mixed with 1 at% of SPD-processed gold. The lack of uniform elongation is typical for most SPD-processed metals [22-25]. With increasing the number of rotations to 10, the yield stress slightly increases (up to 140 MPa), but some significant strain hardening appears and the uniform elongation becomes large (25%). The changes in tensile properties compared to the sample processed with 1 rotation are due to the dissolution of gold in aluminum and the formation of intermetallic phases by mechanical alloying. With a further increase of the HPT strain up to 100 rotations, the yield stress reaches 200 MPa, with still some strain hardening and a uniform elongation of about 15%. With increasing the number of HPT turns up to 1000 (corresponding to the saturation of hardness), the yield stress continues to increase (220 MPa) but there is no more strain hardening and the material does not exhibit uniform elongation anymore.

Examination of fracture surfaces of tensile specimens using SEM is shown in Fig. 9. For the sample processed with 1 rotation, which contains large amounts of unmixed gold and aluminum, features of plastic deformations are observed at low magnification. Examination of this sample at a higher magnification shows the presence of many sharp and long projections elongated in the shear direction. The presence of these elongated projections suggests that this sample after initial plastic deformation fractures by coalescence of voids or cracks through an intergranular mechanism. In this sample, the delamination between the gold and aluminum is also observed, while dimples with small sizes are rarely detected. For the sample processed with 10 turns, some features observed for the sample after 1 turn, such as plastic deformation, delamination and projections in shear direction, are detected. However, a main difference with the sample processed for 1 turn is the presence of small dimples which is and indication of ductile deformation for the sample processed with 1 turn. After 100 turns, the presence of Au-rich and Au-poor layers is evident, delamination does not occur, and numerous tiny dimples with sizes comparable to the grain size are visible. For the sample processed for 1000 turns, the fracture surface is quite smooth, small dimples are visible and numerous nanoparticles of Al_2Au are observed. For both samples processed with 100 and 1000 turns, the presence of dimples with sizes comparable to the grain size suggests that transgranular fracture mechanism can contribute to tensile behavior of these two samples. A main difference between the two samples is that while the sample processed with 1000 turns shows a uniform fracture surface, the sample processed with 100 turns shows a heterogeneous feature due to the plastic strain mismatch between the hard Au-rich and soft Au-poor regions.

A comparison between SEM, TEM and STEM images and tensile testing results suggests that the material with a good combination of strength and ductility exhibits a heterogeneous distribution of Al_2Au nanoscaled particles. Besides the mechanical property evolution of the Al-Au system by HPT processing, its electrical conductivity is also influenced by HPT processing, as discussed in the Appendix A and shown Fig. A1. Taken altogether, the hypothesis of this study was (i) to achieve heterogeneous and homogeneous distributions of nanoscaled particles by HPT processing of Al/Au powder mixtures and ii) to show that the distribution of nanoparticles will affect the mechanical behavior. These two important features will be discussed in the next section.

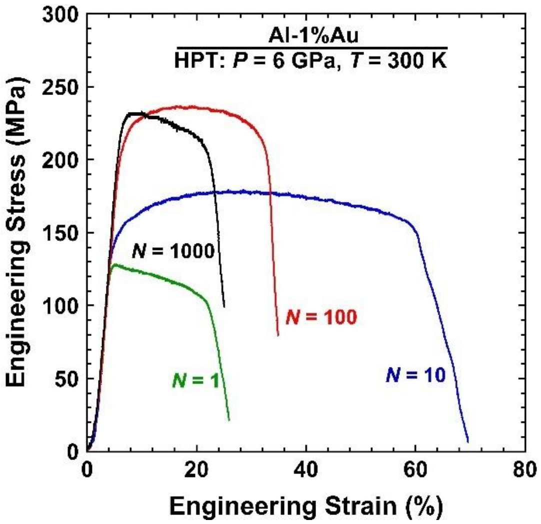

Fig. 8. Nominal tensile stress-strain curves for Al - 1 mol% Au after HPT treatment with 1, 10, 100 and 1000 rotations.

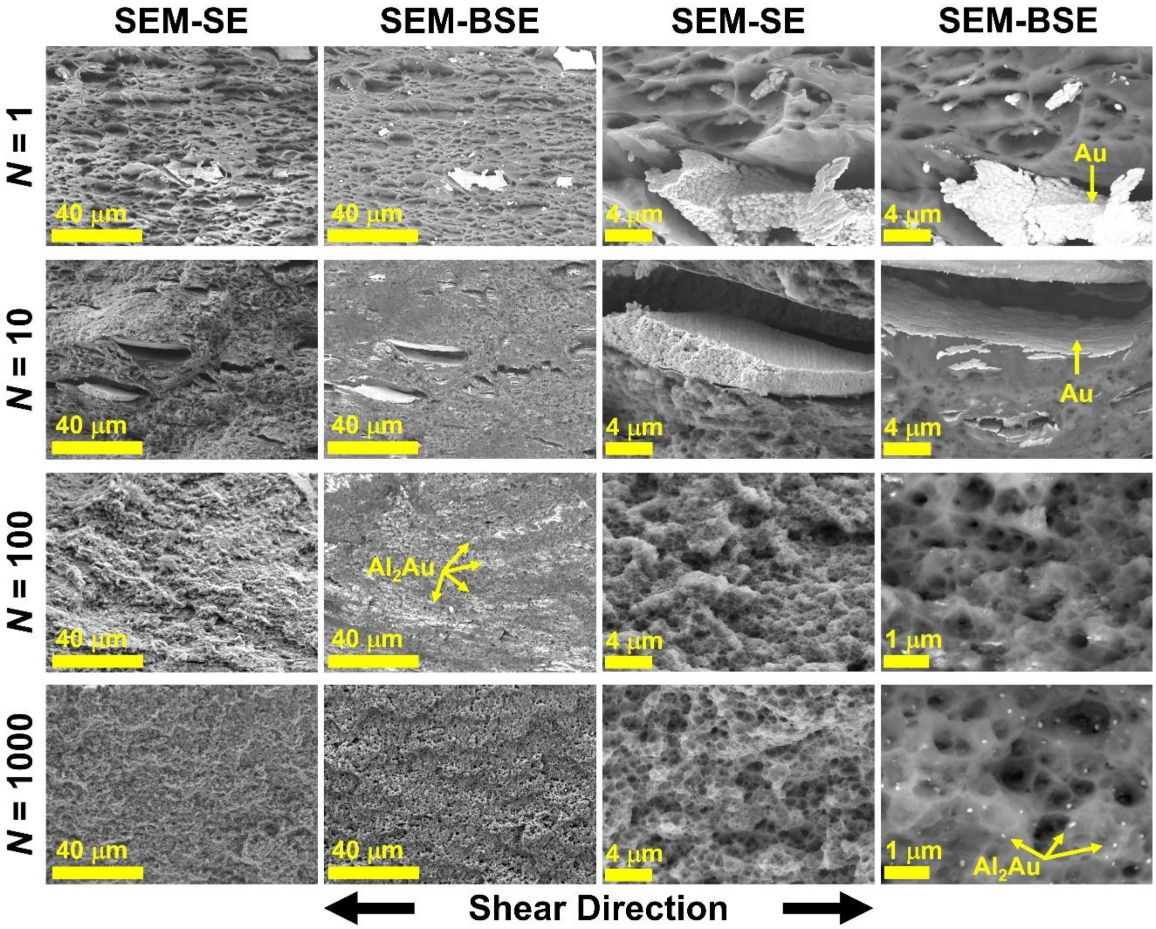

Fig. 9. Fracture surface of tensile specimens fabricated from Al - 1 mol% Au after HPT treatment with 1, 10, 100 and 1000 rotations and pulled to failure. SE and BSE indicate secondary electron and back-scatter electron modes of SEM, respectively.

4. Discussion

This study proposes a unique process to achieve a fine distribution of nanoscaled intermetallic particles within an aluminum matrix. Particles are not created through the classical nucleation and growth process that is widely used for classical precipitate hardening of alloys. It was demonstrated that SPD could be successfully applied for the progressive alloying of aluminum with a small volume fraction of gold, leading to a high density of nanoscaled Al_2Au particles whose distribution was triggered by the strain level. The sample with the heterogeneous distribution of nanoparticles shows a good combination of strength and uniform tensile elongation (indicating a significant strain hardening) while most of the ductility is lost when the distribution of nanoscaled particles becomes homogeneous. Thus, two important features will be discussed in the following: first, the mechanism of formation of nanoparticles and their homogenous/heterogeneous distribution, and second, the strengthening mechanism combined with high ductility.

The multi-phase structure evolution under HPT is schematically represented in Fig. 10. At first, the co-deformation of aluminum and gold leads to the continuous elongation of gold particles and reactive interdiffusion starts at interfaces with the nucleation of intermetallic compounds (AlAu on the gold side and Al_2Au on the aluminum side, Fig. 10a). Then, due to the continuous shear strain during HPT, this intermetallic layer is fragmented, leading to fresh interfaces (Fig. 10b) where the reactive interdiffusion could easily continue to proceed. It also leads to the detachment and dispersion of some nanoparticles with a diameter of about 10 nm, similar to the Al_2Au layer thickness between aluminum and gold (Fig. 10c). Then the process simply continues up to the point where all the gold phase is consumed (Fig. 10d) and at this stage, many Kirkendall voids lie in the middle of former gold grains due to the difference in diffusion coefficients of gold and aluminum. Concomitantly, Al_2Au nanoparticles start to disperse in the aluminum matrix due to the large level of deformation. Thus, they do not exhibit any specific orientation relationships with aluminum grains. Then, the final stage of the interdiffusion reaction (Fig. 10e) is achieved where only the Al_2Au and the FCC aluminum phases (matrix) remain (AlAu phase and Kirkendall voids progressively disappear). Finally, under shear strain, the intermetallic layer becomes so thin that it is fragmented into nanoscaled particles that ultimately disperse in the matrix under further strain, eventually leading to a homogeneous distribution (Fig. 5 and Fig. 6)

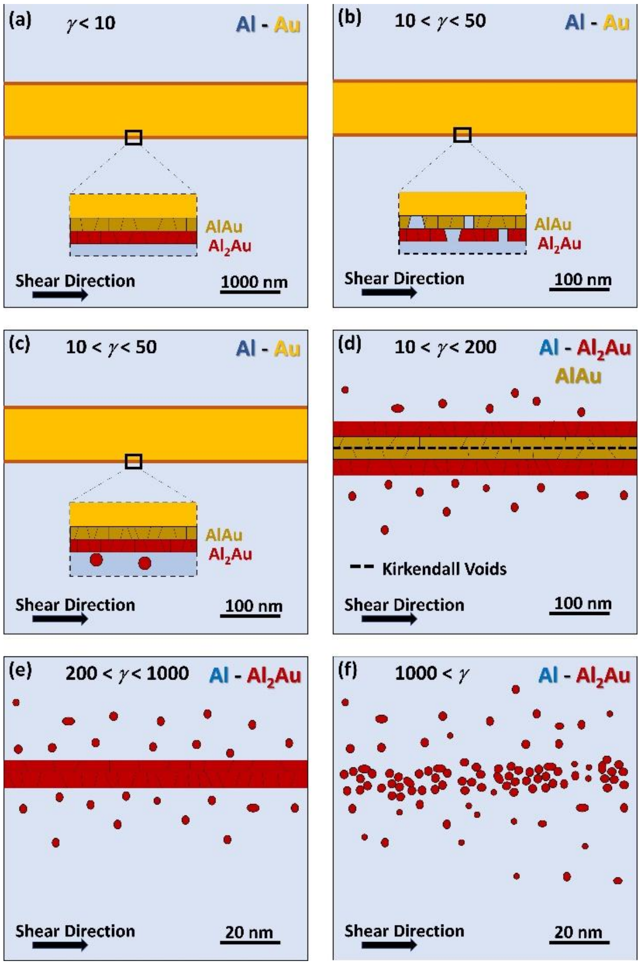

Fig. 10. Schematic representation of the different steps leading to the progressive formation; of nanoscaled Al_2Au particles through reactive interdiffusion at Al/Au interfaces during HPT. (a) Continuous elongation of gold grains under shear and reactive interdiffusion at interfaces (nucleation of intermetallic compounds). (b) Continuous elongation under shear, fragmentation of the intermetallic layer, and creation of fresh interfaces. (c) Continuous elongation under shear, first detachment of some nanoscaled Al_2Au particles and nucleation of new intermetallic compounds. (d) Continuation of the process up to the point where there is no more FCC gold phase, the apparition of significant Kirkendall voids in the middle of former gold grains due to the different diffusion coefficients of gold and aluminum, and the beginning of the dispersion of Al_2Au particles within the aluminum matrix. (e) The final point of the interdiffusion reaction, remaining only the Al_2Au and the FCC Al phases (matrix), and the progressive disappearance of the AlAu phase and Kirkendall voids. (f) The final footprint of the original gold grains fully

transformed into nanoscaled Al_2Au particles, and a gradual transition to homogenization of distribution.

Atomic interdiffusion of aluminum and gold occurred during SPD at room temperature which is evidenced by the formation of intermetallic phases (Al_2Au and AlAu). The reported frequency factor and activation energy for the interdiffusion of gold in aluminum are $D_0 = 2.2\times10^{-4}$ m^2/s and $Q = 134$ kJ/mol, respectively [53]. The interdiffusion at room temperature ($T = 300$ K) can be calculated using an Arrhenius-type equation [55].

$$D = D_0 e^{-Q/RT} \tag{3}$$

where R is the gas constant. This equation suggests an interdiffusion coefficient of $D = 1.0\times10^{-27}$ m^2/s at room temperature. Besides, the diffusion coefficient D can be roughly estimated as [55]

$$D = x^2/t \tag{4}$$

where x is the equivalent diffusion length and t is the time. Since intermetallic layers with a thickness up to 100 nm (Fig. 4) were observed after 10 HPT turns, the diffusion coefficient during HPT processing can be estimated with $x = 10^{-7}$m and $t = 600$ s, leading to $D = 1.5\times10^{-17}$ m^{2}s^{-1}. This is ten orders of magnitude higher than the extrapolation of the diffusion coefficient at room temperature indicating that atomic mobility was significantly promoted by SPD. It has already been reported that atomic diffusion can sometimes be as fast as grain-boundary or surface diffusion in Al-based alloys processed by ultra-SPD [41] due to ultrahigh concentration of point defects and especially vacancies [56,57]. Thus, the fast reactive interdiffusion during SPD is attributed to strain-induced vacancies mostly created in the aluminum matrix (99% volume fraction). Then, due to the different exchange probability between these vacancies with aluminum and gold atoms, many of them end up in the middle of the Au-rich layer forming Kirkendall voids as observed by HAADF STEM (Fig. 4b). The interdiffusion together with shear strain leads to a transition from heterogeneity to homogeneity, however, the final distribution of nanoparticles even after 1000 turns may not be as homogeneous as the one achieved by conventional precipitation hardening process [28,29] due to a large diffusion path of gold atoms.

The specific microstructure evolution in the Al-Au alloy has a strong influence on the tensile behavior (Fig. 8). It is well documented that the heterogeneous distribution of grain sizes in gradient nanostructure materials [8,9], bimodal materials [12,13], and heterostructured materials [26,27] can lead to a good combination of strength and ductility. Coarse-grained regions accommodate the dislocations and give ductility to the material, while nanograined regions are responsible for high strength through the Hall-Petch mechanism [1]. The Al-Au samples processed by 10, 100 and 1000 rotations exhibit ultrafine-grained structures in the aluminum matrix with relatively similar grain sizes (d = 220, 190 and 170 nm, respectively); however, their yield stress is significantly different (σ_Y = 140, 200 and 220 MPa, respectively). The hardening by the Hall-Petch relationship can be estimated through the following equation [58,59].

$$\sigma_{GB} = \sigma_0 + kd_{av}^{-1/2} \tag{5}$$

In this equation, σ_0 is the Peierls-Nabarro stress which is 10 MPa for aluminum and k is the Hall-Petch coefficient which was reported as 0.04 MPa·m$^{1/2}$ [60] or 0.06 MPa·m$^{1/2}$ [61] for aluminum. The Hall-Petch relationship suggests a yield stress of 95-138 MPa for the sample processed by 10 rotations. This indicates that the initial hardening to a yield stress of 140 MPa observed for samples processed with 10 rotations should be mainly due to the Hall-Petch strengthening mechanism, and partly due to dislocation hardening. However, extra hardening observed after 100 and 1000 turns should be due to other strengthening mechanisms. This extra hardening cannot be attributed to dislocation density because XRD peak broadening is reasonably similar for samples processed with 10, 100 and 1000 rotations [47]. It is well documented that the fraction of dislocations increases fast at the early stages of straining, and it remains constant or sometimes decreases due to the contribution of dynamic recovery and recrystallization [48]. Solution hardening can be neglected in this study because the amount of gold in aluminum was only 0.13±0.01 at% and the differences between atomic size mismatch and modulus mismatch of aluminum and gold are not significant [35]. Therefore, extra hardening observed after 100 and 1000 turns should be due to the effect of nanoparticles on pinning the dislocations (similar to Orowan-type precipitation hardening) [20,21].

Regarding ductility, it should be noted that the presence of nanoparticles in optimized fractions can be also beneficial for dislocation accumulation and strain hardening [16,17]. Recent studies suggested that nanoscale precipitates can act as dislocation sources and render uniform ductility of the materials [62]. When the fraction of precipitates is dense and pinning distances are very low, they practically act only as dislocation obstacles, and cannot generate any strain hardening. However, in regions with a lower density of particles, dislocation can proceed [62]. In the current Al-Au alloys, it is then expected that the regions with dense nanoparticles are responsible for high strength, while regions with low density of nanoparticles contribute to high ductility. Such a feature was reported in alloys with bimodal grain sizes [12,13] or heterostructured materials [26,27]. The mechanism underlying a good combination of high strength and high ductility in heterostructured materials was mainly attributed to hetero-deformation-induced strengthening and back stress [63]. When stress is applied to a heterostructured material containing soft and hard regions, the difference between the flow stress of hard and soft regions leads to a strain gradient. This strain gradient accordingly leads to the formation of geometrically necessary dislocations through Frank-Read sources in the soft region to accommodate the strain mismatch. The soft region starts to plastically deform under stress while the hard region resists the deformation. Further accumulation of dislocations by increasing the applied stress results in back stress in soft regions and forward stress in the hard region. The back stress strengthens the soft region and the forward stress contributes to easier deformation of the hard region. Therefore, the soft region shows larger deformation and contribute to high ductility by accumulating the dislocations, while the hard region hinders the dislocation glide and contributes to high strength [26,27]. Although this hetero-deformation-induced strengthening and back stress mechanism could not be experimentally examined in this study due to technical limits, examination of microstructure by high-resolution TEM indicates the capability of ultrafine-grained Al-Au alloys for the accommodation of dislocations, as discussed in Appendix B and shown in Fig. A2.

Taken altogether, although various studies attempted to achieve a good combination of high strength and high ductility by different strategies (twinning [6,7], gradient structures [8,9], lattice softening [10,11], bimodal structure [12,13], lamellar structure [14,15], precipitation [16,17], TWIP [18,19] and TRIP [20,21]), this study suggests that ultrafine-grained alloys with heterogeneous nanoparticle distribution can be considered as a new class of materials with optimized combination of strength and ductility. Although this study was carried out on a model Al-Au alloy and used the specific technique called "ultra-SPD" for synthesis [30,31], the proposed strategy can be potentially realized by optimizing thermochemical routes, as attempted earlier to produce heterostructured materials [26,27]. Finally, it should be noted that although the new Al-Au alloy introduced in this study exhibits an interesting strength-ductility combination, better than many ultrafine-grained or nanostructured metallic alloys, its thermal stability is unfortunately relatively poor, similar to many other SPD-processed materials [23] as discussed in the Appendix A.

5. Conclusions

Motivated by the concept of heterostructured materials, the heterogeneous distribution of nanoparticles was suggested as a strategy to achieve a combination of high strength and high ductility in metallic alloys. To examine this idea, Al-Au alloys were introduced as a new family of aluminum alloys. The heterogeneity was created by the mechanical alloying of aluminum and gold through ultra-severe plastic deformation to achieve Al_2Au nanoparticles in the ultrafine-grained aluminum matrix by fast reactive interdiffusion. For reasonably similar fractions of intermetallic nanoparticles, only the alloys with heterogeneous distribution of particles exhibited strain hardening and high uniform ductility. The achievement of high strength and high ductility by heterogeneous distribution of nanoparticles was attributed to hetero-deformation-induced strengthening and back stress mechanism. These results not only introduce a new strategy to overcome the strength-ductility trade-off in nanostructured metals but also suggest heterogenous precipitation hardening as a future solution to achieve aluminum alloys with high strength and high ductility.

Appendix A

The evolution of electrical conductivity versus hardness is shown in Fig. A1 for discs processed by HPT with 1, 10, 100 and 1000 turns. Moreover, to have an idea about the thermal stability of Al-Au alloys, the sample processed by HPT for 1000 rotations was additionally aged at 373, 423, 473, 523, 573, 623, 673 K for 24 h and examined by Vickers microhardness and electrical conductivity measurements. There is a trade-off relationship between electrical conductivity and hardness, where conductivity decreases and hardness increases after HPT processing. With aging, no precipitation hardening occurs, but a softening and recovery of electrical conductivity are detected. Current data confirm that the thermal stability of the Al-Au alloy is not as high as other nanostructured immiscible Al-based alloys such as Al-Fe [39], Al-Ca [40], Al-Zr [41] and Al-La-Ce [42] processed by ultra-SPD processed. It should be not that poor thermal stability is a general feature of many SPD-processed materials [23].

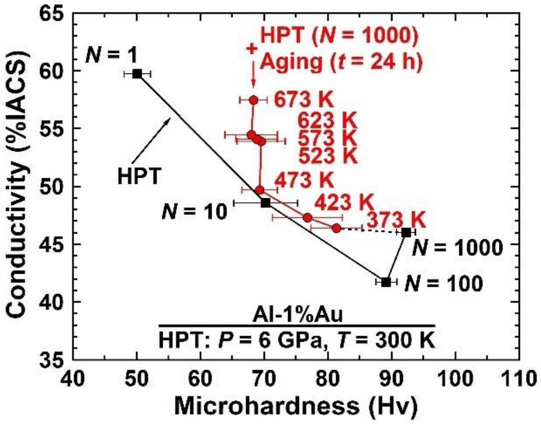

Fig. A1. Variations of electrical conductivity versus microhardness for Al - 1 mol% Au after HPT treatment with 1, 10, 100 and 1000 rotations and after HPT treatment with 1000 rotations followed by aging at different temperatures for 24 h.

Appendix B

Although ultrafine-grained materials cannot usually accommodate dislocations due to the action of grain boundaries as dislocation sinks [5], both individual dislocation and low-angle grain boundaries (dislocation cells) can be detected in Al-Au alloys. Fig. A2 show (a) a high-resolution TEM image of a low angle-grain boundary and (b) lattice image of an individual dislocation for the sample processed by HPT for 10 turns. The capability of the Al-Au alloys for accommodation dislocations should be responsible for their ductility through hetero-deformation-induced work hardening and back stress mechanism [63].

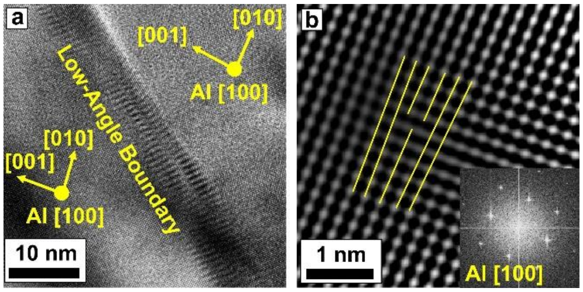

Fig. A2. (a) High-resolution TEM micrograph of a low-angle grain boundary and (b) lattice image of a dislocation for Al - 1 mol% Au after HPT treatment with 10 rotations.

Acknowledgments

This work was supported in part by the Light Metals Educational Foundation of Japan, in part by Grants-in-Aid for Scientific Research from MEXT, Japan (JP19H05176, JP21H00150 and JP22K18737), and in part by the CRNS Federation IRMA - FR 3095.

References

[1] S.N. Naik, S.M. Walley, The Hall–Petch and inverse Hall–Petch relations and the hardness of nanocrystalline metals, J. Materi. Sci. 55 (2020) 2661–2681.

[2] W. Xu, N. Birbilis, G. Sha, Y. Wang, J.E. Daniels, Y. Xiao, M. Ferry, A high-specific-strength and corrosion-resistant magnesium alloy, Nat. Mater. 14 (2015) 1229–1235.

[3] G. Wu, C. Liu, L. Sun, Q. Wang, B. Sun, B. Han, J.J. Kai, J. Luan, C.T. Liu, K. Cao, Y. Lu, L. Cheng, J. Lu, Hierarchical nanostructured aluminum alloy with ultrahigh strength and large plasticity, Nat. Commun. 10 (2019) 5099.

[4] L.M. Kang, C. Yang, A review on high-strength titanium alloys: microstructure, strengthening, and properties, Adv. Eng. Mater. 21 (2019) 1801359.

[5] L.G. Sun, G. Wu, Q. Wang, J. Lu, Nanostructural metallic materials: structures and mechanical properties, Mater. Today 38 (2020) 114-135.

[6] K. Lu, L. Lu, S. Suresh, Strengthening materials by engineering coherent internal boundaries at the nanoscale, Science 324 (2009) 349–352.

[7] X. Liu, L. Sun, L. Zhu, J. Liu, K. Lu, J. Lu, High-order hierarchical nanotwins with superior strength and ductility, Acta Mater. 149 (2018) 397–406.

[8] X. Li, L. Lu, J. Li, X. Zhang, H. Gao, Mechanical properties and deformation mechanisms of gradient nanostructured metals and alloys, Nat. Rev. Mater. 5 (2020) 706–723.

[9] X. Wu, Y. Zhu, K. Lu, Ductility and strain hardening in gradient and lamellar structured materials, Scr. Mater. 186 (2020) 321–325.

[10] T. Saito, T. Furuta, J.H. Hwang, S. Kuramoto, K. Nishino, N. Suzuki, R. Chen, A. Yamada, K. Ito, Y. Seno, T. Nonaka, H. Ikehata, N. Nagasako, C. Iwamoto, Y. Ikuhara, T. Sakuma, Multifunctional alloys obtained via a dislocation-free plastic deformation mechanism, Science 300 (2003) 464–467.

[11] K. Edalati, T. Furuta, T. Daio, S. Kuramoto, Z. Horita, High strength and high uniform ductility in a severely deformed iron alloy by lattice softening and multimodal-structure formation, Mater. Res. Lett. 3 (2015) 197–202.

[12] Y. Wang, M. Chen, F. Zhou, E. Ma, High tensile ductility in a nanostructured metal, Nature 419 (2002) 912–915.

[13] M. Zha, H.M. Zhang, Z.Y. Yu, X.H. Zhang, X.T. Meng, H.Y. Wang, Q.C. Jiang, Bimodal microstructure – a feasible strategy for high-strength and ductile metallic materials, J. Mater. Sci. Technol. 34 (2018) 257–264.

[14] Y. Kimura, T. Inoue, F. Yin, K. Tsuzaki, Inverse temperature dependence of toughness in an ultrafine grain-structure steel, Science 320 (2008) 1057–1060.

[15] L. Fan, T. Yang, Y. Zhao, J. Luan, G. Zhou, H. Wang, Z. Jiao, C.T. Liu, Ultrahigh strength and ductility in newly developed materials with coherent nanolamellar architectures, Nat. Commun. 11 (2020) 6240.

[16] Z. Horita, K. Ohashi, T. Fujita, K. Kaneko, T.G. Langdon, Achieving high strength and high ductility in precipitation-hardened alloys, Adv Mater. 17 (2005) 1599–1602.

[17] S.H. Kim, H. Kim, N.J. Kim, Brittle intermetallic compound makes ultrastrong low-

density steel with large ductility, Nature 518 (2015) 77–79.

[18] M. Schinhammer, C.M. Pecnik, F. Rechberger, A.C. Hanzi, J.F. Loffler, P.J. Uggowitzer, Recrystallization behavior, microstructure evolution and mechanical properties of biodegradable Fe-Mn-C(-Pd) TWIP alloys, Acta Mater. 60 (2012) 2746–2756.

[19] B.C. De Cooman, Y. Estrin, S.K. Kim, Twinning-induced plasticity (TWIP) steels, Acta Mater. 142 (2018) 283–362.

[20] B. Ellyson, J. Klemm-Toole, K. Clarke, R. Field, M. Kaufman, A. Clarke, Tuning the strength and ductility balance of a TRIP titanium alloy, Scr. Mater. 194 (2021) 113641.

[21] C. Hu, C.P. Huang, Y.X. Liu, A. Perlade, K.Y. Zhu, M.X. Huang, The dual role of TRIP effect on ductility and toughness of a medium Mn steel, Acta Mater. 245 (2023) 118629.

[22] R.Z. Valiev, Y. Estrin, Z. Horita, T.G. Langdon, M.J. Zehetbauer, Y.T. Zhu, Producing bulk ultrafine-grained materials by severe plastic deformation, JOM 58 (2006) 33–39.

[23] K. Edalati, A. Bachmaier, V.A. Beloshenko, Y. Beygelzimer, V.D. Blank, W.J. Botta, K. Bryła, J. Čížek, S. Divinski, N.A. Enikeev, Y. Estrin, G. Faraji, R.B. Figueiredo, M. Fuji, T. Furuta, T. Grosdidier, J. Gubicza, A. Hohenwarter, Z. Horita, J. Huot, Y. Ikoma, M. Janeček, M. Kawasaki, P. Krǎl, S. Kuramoto, T.G. Langdon, D.R. Leiva, V.I. Levitas, A. Mazilkin, M. Mito, H. Miyamoto, T. Nishizaki, R. Pippan, V.V. Popov, E.N. Popova, G. Purcek, O. Renk, Á. Révész, X. Sauvage, V. Sklenicka, W. Skrotzki, B.B. Straumal, S. Suwas, L.S. Toth, N. Tsuji, R.Z. Valiev, G. Wilde, M.J. Zehetbauer, X. Zhu, Nanomaterials by severe plastic deformation: review of historical developments and recent advances, Mater. Res. Lett. 10 (2022) 163–256.

[24] P. Kumar, M. Kawasaki, T.G. Langdon, Review: Overcoming the paradox of strength and ductility in ultrafine-grained materials at low temperatures, J. Mater. Sci. 51 (2016) 7-18.

[25] A. Ovid'ko, R.Z. Valiev, Y.T. Zhu, Review on superior strength and enhanced ductility of metallic nanomaterials, Prog. Mater. Sci. 94 (2018) 642–540.

[26] L. Romero-Resendiz, M. Naeem, Y.T. Zhu, Heterostructured materials by severe plastic deformation: overview and perspectives, Mater. Trans. 64 (2023) 2346–2360.

[27] Y. Zhu, K. Ameyama, P.M. Anderson, I.J. Beyerlein, H. Gao, H.S. Kim, E. Lavernia, S. Mathaudhu, H. Mughrabi, R.O. Ritchie, N. Tsuji, X. Zhang, X. Wu, Heterostructured materials: superior properties from hetero-zone interaction, Mater. Res. Lett. 9 (2020) 1–31.

[28] W.J. Poole, X. Wang, D.J. Lloyd, J.D. Embury, The shearable-non-shearable transition in Al-Mg-Si-Cu precipitation hardening alloys: implications on the distribution of slip, work hardening and fracture, Philos. Mag. 85 (2005) 3131-3135.

[29] T.T. Sasaki, K. Oh-ishi, T. Ohkubo, K. Hono, Enhanced age hardening response by the addition of Zn in Mg-Sn alloys, Scr. Mater. 55 (2006) 251-254.

[30] F.R. Brotzen, C.T. Rosemayer, R.J. Gale, Mechanical behavior of aluminum and Al-Cu(2%) thin films, Thin Solid Films 166 (1988) 291-298.

[31] Y.L. Zhao, T. Yang, Y. Tong, J. Wang, J.H. Luan, Z.B. Jiao, D. Chen, Y. Yang, A. Hu, C.T. Liu, J.J. Kai, Heterogeneous precipitation behavior and stacking-fault-mediated deformation in a CoCrNi-based medium-entropy alloy, Acta Mater. 138 (2017) 72-82.

[32] Z.Y. Jia, S.Z. Zhang, J.T. Huo, C.J. Zhang, L.W. Zheng, F.T. Kong, H. Li, Heterogeneous precipitation strengthened non-equiatomic NiCoFeAlTi medium entropy alloy with excellent mechanical properties, Mater. Sci. Eng. A 834 (2022) 142617.

[33] M. Moshref-Javadi, S.H. Seyedein, M.T. Salehi, M.R. Aboutalebi, Age-induced multi-stage transformation in a Ni-rich NiTiHf alloy, Acta Mater.61 (2013) 2583-2594.

[34] S. Sarkar, C.S. Kumar, A.K. Nath, Effect of different heat treatments on mechanical properties of laser sintered additive manufactured parts, J. Manuf. Sci. Eng. 139 (2017) 111010.

[35] J.L. Murray, H. Okamoto, T.B. Massalski, The Al-Au (aluminum-gold) system, Bull. Alloy Phase Diag. 8 (1987) 20–30.

[36] X. Sauvage, A. Duchaussoy, G. Zaher, Strain induced segregations in severely deformed materials, Mater. Trans. 60 (2019) 1151–1158.

[37] K. Edalati, R. Uehiro, K. Fujiwara, Y. Ikeda, H.W. Li, X. Sauvage, R.Z. Valiev, E. Akiba, I. Tanaka, Z. Horita, Ultra-severe plastic deformation: evolution of microstructure, phase transformation and hardness in immiscible magnesium-based systems, Mater. Sci. Eng. A 701 (2017) 158–166.

[38] K. Edalati, Metallurgical alchemy by ultra-severe plastic deformation via high-pressure torsion process, Mater. Trans. 60 (2019) 1221–1229.

[39] A. Duchaussoy, X. Sauvage, K. Edalati, Z. Horita, G. Renou, A. Deschamps, F. De Geuser, Structure and mechanical behavior of ultrafine-grained aluminum-iron alloy stabilized by nanoscaled intermetallic particles, Acta Mater. 167 (2019) 89–102.

[40] X. Sauvage, F. Cuvilly, A. Russell, K. Edalati, Understanding the role of Ca segregation on thermal stability, electrical resistivity and mechanical strength of nanostructured aluminum, Mater. Sci. Eng. A 798 (2020) 140108.

[41] A. Mohammadi, N.A. Enikeev, M.Y. Murashkin, M. Arita, K. Edalati, Developing age-hardenable Al-Zr alloy by ultra-severe plastic deformation: significance of supersaturation, segregation and precipitation on hardening and electrical conductivity, Acta Mater.203 (2021) 116503.

[42] A. Mohammadi, N.A. Enikeev, M.Y. Murashkin, M. Arita, K. Edalati, Examination of inverse Hall-Petch relation in nanostructured aluminum alloys by ultra-severe plastic deformation, J. Mater. Sci. Technol. 91 (2021) 78–89.

[43] A.P. Zhilyaev, T.G. Langdon, Using high-pressure torsion for metal processing: fundamentals and applications, Prog. Mater. Sci. 53 (2008) 893-979.

[44] R. Pippan, S. Scheriau, A. Taylor, M. Hafok, A. Hohenwarter, A. Bachmaier, Saturation of fragmentation during severe plastic deformation, Annu. Rev. Mater. Res. 40 (2010) 319-343.

[45] M. Kawasaki, R. Figueiredo, Y. Huang, T.G. Langdon, Interpretation of hardness evolution in metals processed by high-pressure torsion, *J. Mater. Sci.* 49 (2014) 6586-6596.

[46] K. Edalati, Z. Horita, A review on high-pressure torsion (HPT) from 1935 to 1988, Mater. Sci. Eng. A 652 (2016) 325-352.

[47] K. Nakagawa, M. Hayashi, K. Takano-Satoh, H. Matsunaga, H. Mori, K. Maki, Y. Onuki, S. Suzuki, S. Sato, Characterization of dislocation rearrangement in FCC metals during work hardening using X-ray diffraction line-profile analysis, Quantum Beam Sci. 4 (2020) 36.

[48] J. Gubicza, Lattice defects and their influence on the mechanical properties of bulk materials processed by severe plastic deformation, Mater. Trans. 60 (2019) 1230-1242.

[49] G. Wilde, S. Divinski, Grain boundaries and diffusion phenomena in severely deformed materials, Mater. Trans. 60 (2019) 1302-1315.

[50] K. Edalati, H. Shao, H. Emami, H. Iwaoka, Z. Horita, E. Akiba, Activation of titanium-vanadium alloy for hydrogen storage by introduction of nanograins and edge dislocations

using high-pressure torsion, Int. J. Hydrog. Energy 41 (2016) 8917-8924.

[51] K. Edalati, Superfunctional materials by ultra-severe plastic deformation, Materials 16 (2023) 587.

[52] S.W. Chee, Z.M. Wong, Z. Baraissov, S.F. Tan, T.L. Tan, U. Mirsaidov, Interface-mediated Kirkendall effect and nanoscale void migration in bimetallic nanoparticles during interdiffusion, Nat. Commun. 10 (2019) 2831.

[53] M. O, M. Kajihara, Kinetics of solid-state reactive diffusion between Au and Al, Mater. Trans.52 (2011) 677-684.

[54] N. Kamikawa, N. Tsuji, Microstructure and mechanical properties of ARB processed aluminium with different purities, Mater. Trans. 57 (2016) 1720-1728.

[55] H. Mehrer, Numerical Data and Functional Relationship in Science and Technology, Vol. 26, Diffusion in Solid Metals and Alloys, Springer, Berlin, 1990.

[56] D. Setman, E. Schafler, E. Korznikova, M.J. Zehetbauer, The presence and nature of vacancy type defects in nanometals detained by severe plastic deformation, Mater. Sci. Eng. A 493 (2008) 116-122.

[57] J. Cizek, M. Janecek, T. Vlasak, B. Smola, O. Melikhova, R.K. Islamgaliev, S.V. Dobatkin, The development of vacancies during severe plastic deformation, Mater. Trans. 60 (2019) 1533-1542.

[58] E. Hall: The deformation and ageing of mild steel: III discussion of results, Proc. Phys. Soc., B 64 (1951) 747-752.

[59] N.J. Petch: The orientation relationships between cementite and α-iron, Acta Cryst. 6 (1953) 96-96.

[60] N. Hansen, Hall–Petch relation and boundary strengthening, Scr. Mater. 51 (2004) 801-806.

[61] S. Thangaraju, M. Heilmaier, B.S. Murty, S.S. Vadlamani, On the estimation of true Hall–Petch constants and their role on the superposition law exponent in Al Alloys, Adv. Eng. Mater. 14 (2012) 892-897.

[62] S. Peng, Y. Wei,H. Gao, Nanoscale precipitates as sustainable dislocation sources for enhanced ductility and high strength, PANS 117 (2020) 5204-5209.

[63] Y. Zhu, X. Wu, Perspective on hetero-deformation induced (HDI) hardening and back stress, Mater. Res. Lett. 7 (2019) 393-398.